

# Corrosion evaluation of welded nickel aluminum bronze and manganese aluminum bronze in synthetic sea water

Ignacio Cobo<sup>1</sup>  | Maria V. Biezma-Moraleda<sup>1</sup>  | Paul Linhardt<sup>2</sup> 

<sup>1</sup>Departamento de Ciencia e Ingeniería del Terreno y de los Materiales, E.T.S. Náutica, Universidad de Cantabria, Santander, Spain

<sup>2</sup>Institute of Chemical Technologies and Analytics, Technische Universität Wien, Vienna, Austria

## Correspondence

Ignacio Cobo, Departamento de Ciencia e Ingeniería del Terreno y de los Materiales, E.T.S. Náutica, Universidad de Cantabria, Santander 39004, Spain.  
Email: [ignacio.cobo@alumnos.unican.es](mailto:ignacio.cobo@alumnos.unican.es)

## Funding information

Universidad de Cantabria,  
Grant/Award Number: 03.DI07.649

## Abstract

Nickel aluminum bronze (NAB) and manganese aluminum bronze (MAB) are highly alloyed bronzes that are increasingly employed in several industrial sectors mainly related to the hostile environment due to their excellent resistance against corrosion, cavitation, erosion, and improved mechanical properties in comparison with other copper-based alloys. These materials are sensitive to thermal treatments, such as welding, due to a multiphase microstructure in cast conditions. To contribute to the knowledge of the behavior of both alloys, the effect of welding processes on the corrosion behavior of NAB (CuAl10Fe5Ni5) and MAB (CuMn12Al8Fe4Ni2) is studied. As the microstructures of the parent zone (PZ), heat-affected zone (HAZ), and weld seam (WS) may be quite different, the consequences with respect to corrosion behavior must be considered. In this study, the influence on corrosion behavior in synthetic sea water (SSW) was investigated using different welded test coupons representing identical (symmetrical) and hybrid joints of NAB and MAB. The microstructures of the welded samples were characterized by metallography using two chemical agents and examined by optical and scanning electron microscopy. By electrochemical corrosion testing, the major effect of welding processes on the corrosion behavior was found in influencing the amount and distribution of  $\beta$ -phase which is prone to selective corrosion.

## KEYWORDS

corrosion test, manganese aluminum bronze, microstructure, nickel aluminum bronze, synthetic sea water, weld

## 1 | INTRODUCTION

Nickel aluminum bronzes (NAB) and manganese aluminum bronzes (MAB) are copper-based alloys with relevant content of Ni, Al, Mn, and Fe. Besides good mechanical properties, they have high resistance to corrosion in

numerous environments, particularly marine conditions, and excellent tribological behavior, such as resistance against erosion, wear, and cavitation. These properties make them highly versatile alloys and the basic fields of application are linked to the manufacture of valves, turbines, and marine propellers.<sup>[1–4]</sup> The propeller's

This is an open access article under the terms of the Creative Commons Attribution-NonCommercial-NoDerivs License, which permits use and distribution in any medium, provided the original work is properly cited, the use is non-commercial and no modifications or adaptations are made.

© 2022 The Authors. *Materials and Corrosion* published by Wiley-VCH GmbH.

manufacturing methods frequently include fixing the blades to the hub or boss through welding or forging, yielding one object, finally. In some cases, blades and hubs are made of different materials such as NAB and MAB.<sup>[5]</sup>

The fundamental difference between both alloys is manifested mainly in the content of Mn and to a lesser extent in the percentages of Ni and Fe.<sup>[6,7]</sup> The two bronzes are similar in many aspects as is shown in this study, but there are also important differences. In brief, MAB has better welding, hot-working, and casting properties, and offers competitive costs mainly due to its lower Ni content, but its resistance to corrosion is inferior compared to NAB.

Both alloys present high microstructural complexity which is a direct consequence of the chemical composition and the possible thermal treatments they may undergo.<sup>[8–15]</sup> Besides the cooling inherent to the solidification process itself during casting, further thermal influences may occur during the manufacturing or in service, and particularly welding is one of the most relevant with important consequences on the corrosion behavior of these alloys.<sup>[16–19]</sup>

The microstructure of NAB and MAB consists of  $\alpha$ -phase,  $\beta$ -phase, and multishaped intermetallic  $\kappa$  precipitates.<sup>[20–23]</sup> As the  $\beta$ -phase is the most reactive one and it corrodes by de-alloying<sup>[21,24–26]</sup> that may propagate widely until the component is deteriorated, leading to a service failure in some cases,<sup>[27–30]</sup> it must be concluded that NAB and MAB propellers are to some degree susceptible to marine corrosion. It is a usual practise to repair a blade with defects as a result of the casting process or due to service conditions, being the overlay welding the common and economical method for repairing damaged ship propellers made from NAB or MAB.<sup>[31]</sup>

In a weld, the microstructures of the parent zone (PZ), the weld seam (WS), and the heat-affected zone (HAZ) may be quite different. It was reported that the HAZ of different welds were corroded more rapidly than both, PZ and WS, mainly due to the presence of precipitates, dislocations, stacking faults, or defects.<sup>[32,33]</sup> Such defects tend to allocate along grain and phase boundaries enhancing disorder and elemental diffusion.<sup>[34–40]</sup> However, the corrosion behavior specifically of MAB and the combination between NAB and MAB in hybrid weld joints, and repair welding of these two bronze alloys have not yet been thoroughly investigated. One difficulty of welding NAB and MAB components is the lack of understanding of microstructural development in the HAZ and its possible impact on corrosion behavior.

The aim of this contribution was to study the process of microstructure evolution and investigate the corrosion behavior of NAB and MAB welded specimens, considering similar materials, that is, NAB-NAB and MAB-MAB,

and in hybrid joints, that is, NAB-MAB, with two different filler metals in synthetic sea water (SSW). It was assumed that not only the chemical composition but also the microstructures of NAB and MAB can have strong effects on the corrosion behavior and the knowledge gained would possibly permit to improve corrosion resistance after welding of such high-cost marine propellers by focusing attention on the effect of HAZ microstructure.

## 2 | EXPERIMENTAL PROCEDURES

### 2.1 | Specimen preparation

The chemical compositions of the studied bronze alloys NAB, MAB, and the used filler materials (ERCuNiAl, ERCuMnNiAl) are presented in Table 1. As received, as-cast samples of both alloys were welded in pairs obtaining the following coupons: NAB-NAB with ERCuNiAl filler, MAB-MAB with ERCuMnNiAl filler, and NAB-MAB with both filler metals. One-pass tungsten inert gas (TIG) welding process under argon (5–10 L/min) was applied with a voltage of 12 V and a current of 50 A at a speed of 100 mm/min. The cut coupons finally received were  $20 \times 20 \times 3$  mm<sup>3</sup> in size with a 20 mm long WS in the middle, as shown in Figure 1. These coupons were

**TABLE 1** Chemical composition of NAB and MAB as provided by the foundry, and the nominal composition of the filler metals (wt%).

	Cu	Al	Ni	Fe	Mn	Zn	Pb	Si
NAB	Bal.	9.31	4.57	4.92	1.23	0.05	0.05	0.04
MAB	Bal.	7.03	2.21	3.82	12.50	2.13	0.02	0.08
ERCuNiAl	Bal.	9.00	5.00	4.00	1.50	0.10	0.02	0.20
ERCuMnNiAl	Bal.	7.50	2.00	3.00	12.50	0.10	0.02	0.10

Abbreviations: MAB, manganese aluminum bronze; NAB, nickel aluminum bronze.

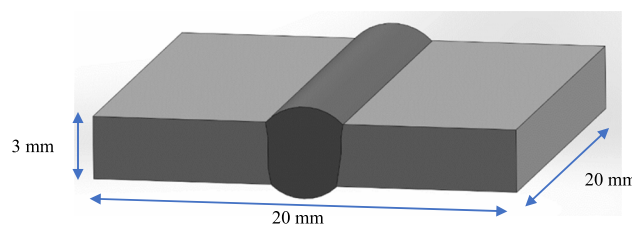


**FIGURE 1** Schematic illustration of the single-pass tungsten inert gas welding over two bronze alloy pieces showing dimensions. [Color figure can be viewed at [wileyonlinelibrary.com](https://onlinelibrary.wiley.com/doi/10.1002/maco.202213338)]

cut perpendicular to the WS into 3 mm wide and 20 mm long slices with the weld in the middle position. Such specimens were used for metallographic investigation of the cross-section before and after electrochemical corrosion tests.

## 2.2 | Metallographic preparation

The sectioned samples were prepared for metallographic characterization by embedding in phenolic resin and stepwise grinding from 320 to 1000 grit SiC, followed by polishing steps with 9 and 3 m diamond and 0.05  $\mu\text{m}$  alumina suspensions. To reveal the microstructures, two different solutions were used referenced as etchant 1 and etchant 2: ferric chloride (5 g  $\text{FeCl}_3$ , 20 ml HCl, and 80 ml distilled water) and ammonium hydroxide (25 ml  $\text{NH}_4\text{OH}$ , 25 ml  $\text{H}_2\text{O}_2$ , and 25 ml distilled water), during 10 and 13 s, respectively.<sup>[41,42]</sup> Metallographic analyses were performed with a light optical microscope (LOM; Leica DM 100; Leica Mikrosysteme Vertrieb GmbH) and a scanning electron microscope (SEM, JEOL 2000; JEOL Ltd.) equipped with energy dispersive spectroscopy (EDS) and backscattered electron detector (BSE).

## 2.3 | Electrochemical corrosion testing

SSW was prepared according to the standard DIN 50905-4, by dissolving the respective amounts of NaCl,  $\text{NaHCO}_3$ ,  $\text{Na}_2\text{SO}_4$ ,  $\text{MgCl}_2 \cdot 6\text{H}_2\text{O}$ , and  $\text{CaCl}_2 \cdot 2\text{H}_2\text{O}$  in deionized water. Potentiostatic corrosion tests were carried out in a cylindrical container (ca. 300 mm diameter) serving as a test cell and filled with 6 L of electrolyte. A cylinder made from stainless steel mesh was placed inside along the container wall, serving as a counter electrode (CE). The reference electrode (RE) was inserted from the top in the center of the container. For each test, four samples, serving as working electrodes (WE), were contacted by clamping to suitably bent stainless steel wires and placed symmetrically around the RE. The NAB-NAB and MAB-MAB samples were polarized to  $-250$ ,  $-200$ ,  $-150$ , and  $-100$  mV<sub>SCE</sub>, and, as a consequence of the results, the NAB-MAB to  $-300$ ,  $-250$ ,  $-200$ , and  $-150$  mV<sub>SCE</sub>. The lowest of these values was estimated to be close to the open circuit potential of each bronze alloy in SSW and is based on practical experience. The most positive potential was selected to be at or above the limit of the passive range, that is, in the range of active metal dissolution. Polarization was controlled by a multichannel potentiostat (Octopoti, homemade), connected to a data acquisition system logging the individual currents up to 72 h.<sup>[43]</sup>

The total surface area was considered for all specimens for calculating the current density. However, due to the heterogeneous character of the surface and the different zones (WS/HAZ/PZ), the geometric configuration of the cross-section according to Figure 1 must be taken into account when interpreting these current densities.

## 3 | RESULTS AND DISCUSSION

### 3.1 | Characterization of the as-welded specimens

The microstructure of the NAB-NAB and MAB-MAB weld joints are shown in Figures 2 and 3 by means of LOM and SEM. In the general views of the welds (Figures 2a and 3a) appear three zones along the weld divided by microstructure: PZ, HAZ, and WS. Etchant 1 was the best to reveal the microstructure of NAB, while etchant 2 was found to be the best to reveal the phases of MAB. Figure 4 shows the microstructure of the NAB-MAB hybrid weld joint with ERCuMnNiAl and ERCu-NiAl fillers with etchant 1. The microstructure of hybrid weld samples did not reveal further details than the information from the symmetrical ones. Consequently, for hybrid joints, we report only on the electrochemical corrosion tests and the subsequent microstructure analysis of the corroded surface.

The PZ of NAB (Figure 2b), shows a complex columnar microstructure, with a high percentage of bright  $\alpha$ -phase dendrites, and a dark zone corresponding to the  $\beta$ -phase. In addition, a series of small micro-precipitates corresponding to the  $\kappa$ -phases are observed as black dots located in the  $\alpha$ -phase and at the interface between  $\alpha$ - and  $\beta$ -phases (Figure 2e). On the other hand, the PZ of MAB (Figure 3e) shows a globular zone with a predominant bright  $\alpha$ -phase and the just gradually darker  $\beta$ -phase. Moreover, precipitates of rosette-shaped  $\kappa$ -phases, corresponding to the  $\kappa_{\text{I}}$ -phase, are observed in gray color and their size is larger than those found in the NAB. Small precipitates corresponding to the  $\kappa_{\text{II}}$ -phase are observed as dark dots in Figure 3e, mostly in the  $\beta$ -phase and at the  $\alpha/\beta$  interface.

The HAZ of NAB (Figure 2c) shows a more complex microstructure than the PZ, with a high percentage of dendrites, where two kinds of dendrites with different morphologies can be distinguished: the typical thick arms of  $\alpha$ -phase dendrites from a faster cooling rate, and needle-shaped so-called  $\alpha$  Widmanstätten structure, typically the consequence of slower cooling rates.<sup>[16]</sup> The dark zone corresponds to the  $\beta$ -phase, and the  $\kappa$ -phases are located mainly at the  $\alpha/\beta$  interface and have

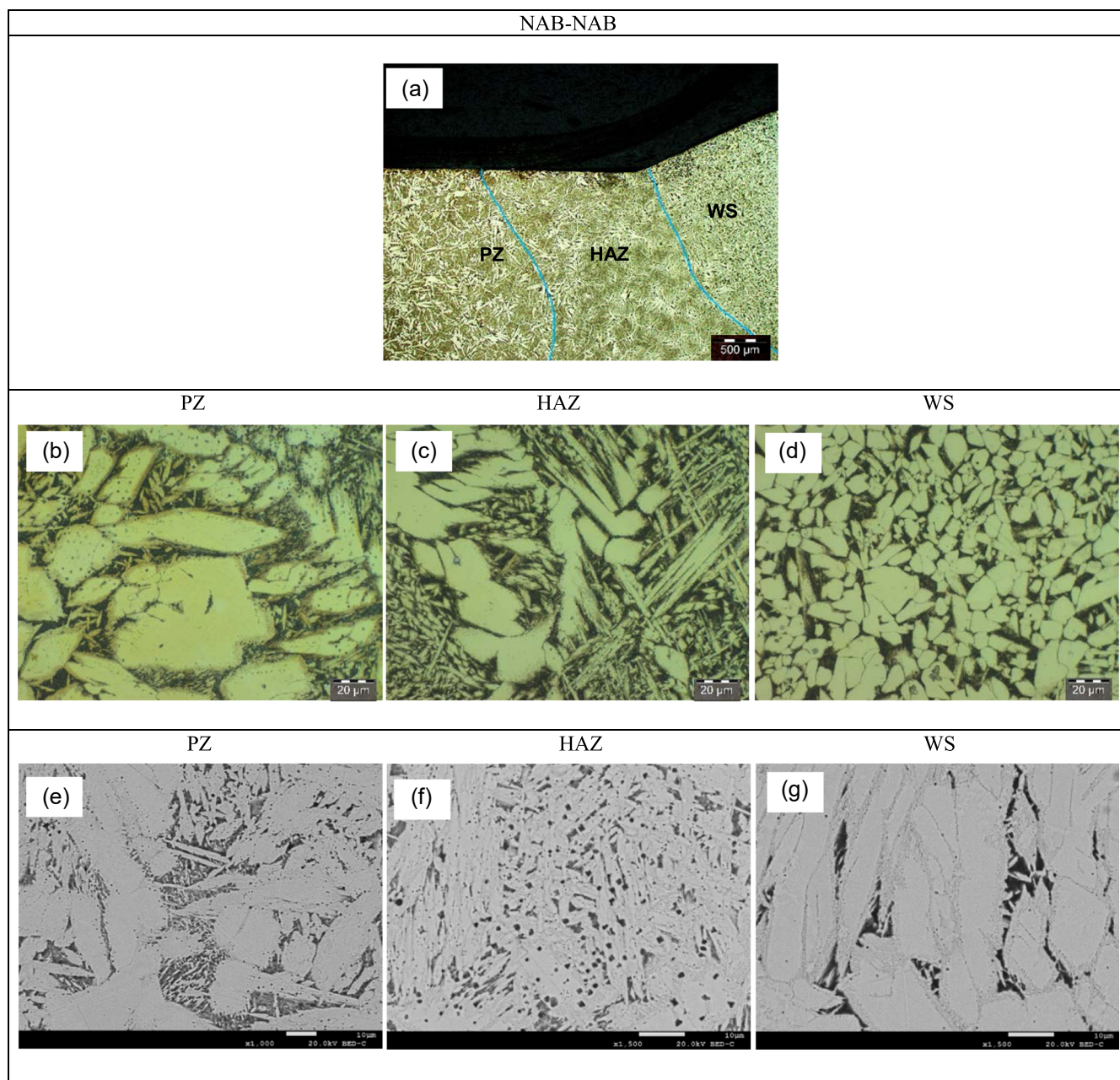


**FIGURE 2** LOM images after applying etchant 1 showing an overview of the microstructure of the NAB-NAB weld joint with ER CuNiAl filler: (a) general view, (b) PZ, (c) HAZ, and (d) WS; SEM-BSE images of (e) PZ, (f) HAZ and (g) WS. BSE, backscattered electron; HAZ, heat-affected zone; LOM, light optical microscope; NAB, nickel aluminum bronze; PZ, parent zone; SEM, scanning electron microscope; WS, weld seam. [Color figure can be viewed at [wileyonlinelibrary.com](https://onlinelibrary.wiley.com/doi/10.1002/maco.202213338)]

increased in size compared to PZ (Figure 2f). The microstructure of the HAZ of MAB (Figure 3c) shows an increased density of needle-shaped  $\alpha$ -phase. On the other hand, the  $\kappa_I$ - and  $\kappa_{II}$ -phases continue to be present homogeneously distributed inside the  $\alpha$ - and  $\beta$ -phase, and at the  $\alpha/\beta$  interface, respectively (Figure 3f).

The WS of NAB (Figure 2d) presents a clear refinement of the  $\alpha$ -phase in the form of equiaxial grains and the Widmanstatten structure has disappeared. The amount of  $\kappa$ -phases is smaller in this microstructure,

compared to PZ (Figure 2g). The microstructure of the WS of MAB (Figure 3d) shows a notable higher content in  $\beta$ -phase, compared to PZ. Small precipitates are observed, mostly in the  $\beta$ -phase and in the  $\alpha/\beta$  interface, referenced as  $\kappa_{II}$  phases. In the WS, the  $\kappa_I$ -phase appears absent (Figure 3g), leaving the structure only as  $\alpha$ -phase,  $\beta$ -phase, and the microprecipitates of  $\kappa_{II}$ -phases, as was also reported previously.<sup>[44]</sup> In general, the microstructure of the HAZ and the WS are found very similar, and sometimes it is easy to confuse them

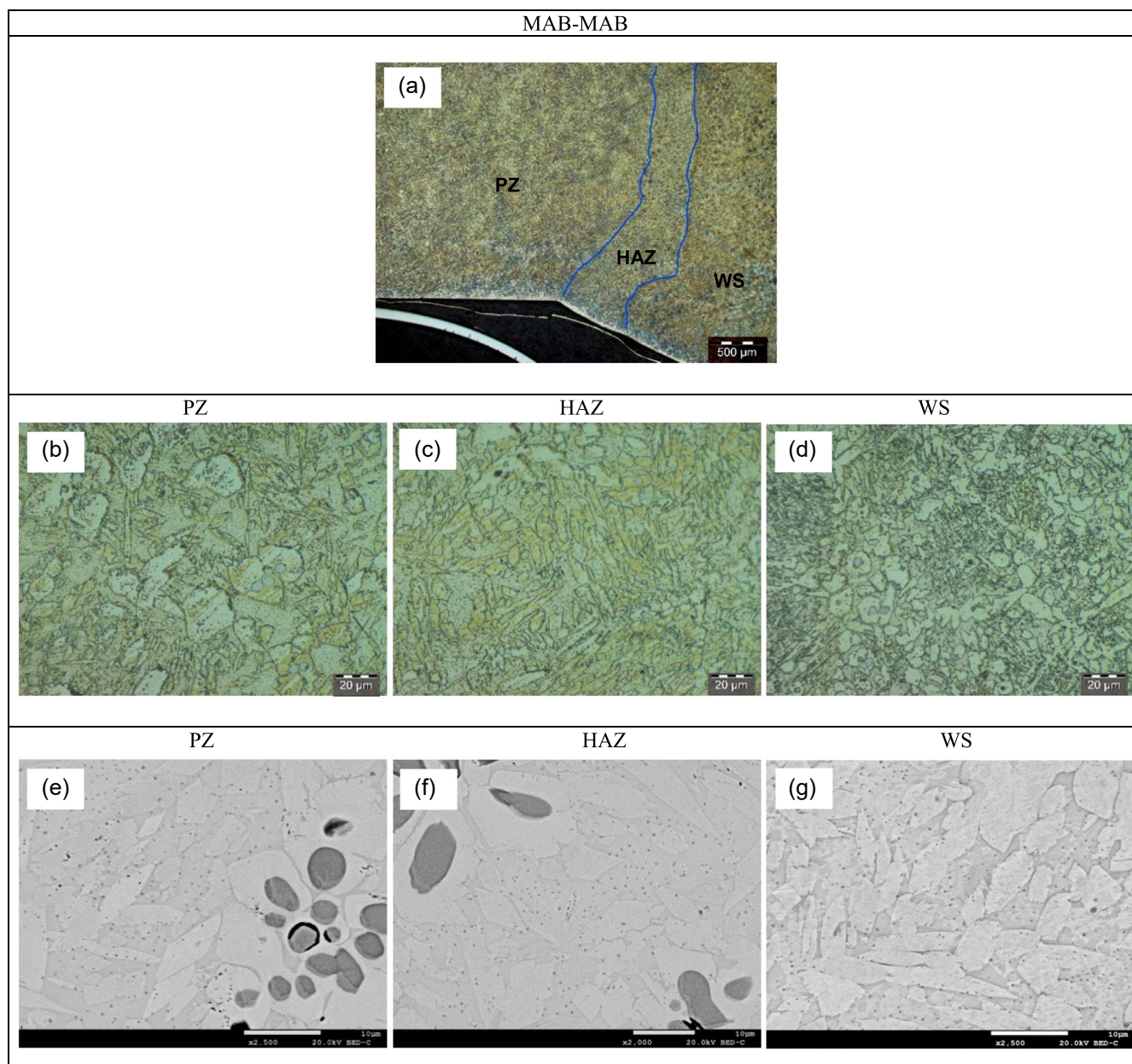


**FIGURE 3** LOM images after applying etchant 2 showing an overview of the microstructure of the MAB-MAB weld joint with ERCuMnNiAl filler: (a) general view, (b) PZ, (c) HAZ, and (d) WS; SEM-BSE images of (e) PZ, (f) HAZ, and (g) WS. BSE, backscattered electron; HAZ, heat-affected zone; LOM, light optical microscope; MAB, manganese aluminum bronze; PZ, parent zone; SEM, scanning electron microscope; WS, weld seam. [Color figure can be viewed at [wileyonlinelibrary.com](https://onlinelibrary.wiley.com/doi/10.1002/maco.202213338)]

depending on which zone is observed, corroborating previous studies.<sup>[45]</sup>

The microstructure of the NAB-MAB hybrid weld joint (Figure 4) shows good, defect-free weldability of the two materials. Despite the different chemical compositions of the fillers, a homogenous microstructure at the fusion line is observed on the NAB side (Figure 4a,c), and the different zones are clearly separated. By contrast, on the MAB side (Figure 4b,d), the different zones, WS, HAZ, and PZ, appear microstructurally unseparated, making it difficult to identify them, specifically the HAZ.

### 3.2 | Electrochemical corrosion tests

Potentiostatic corrosion test results of NAB and MAB weld joints are presented in Figures 5 and 6. The NAB-NAB weld joint exhibits stable passive behavior at potentials up to  $-150 \text{ mV}_{\text{SCE}}$  as indicated by the drop of the respective currents during the test duration to very low final levels. At  $-100 \text{ mV}_{\text{SCE}}$ , however, the anodic current density remains high, the metal dissolves at a high rate throughout the test and the transpassive state may be concluded (Figure 5a).

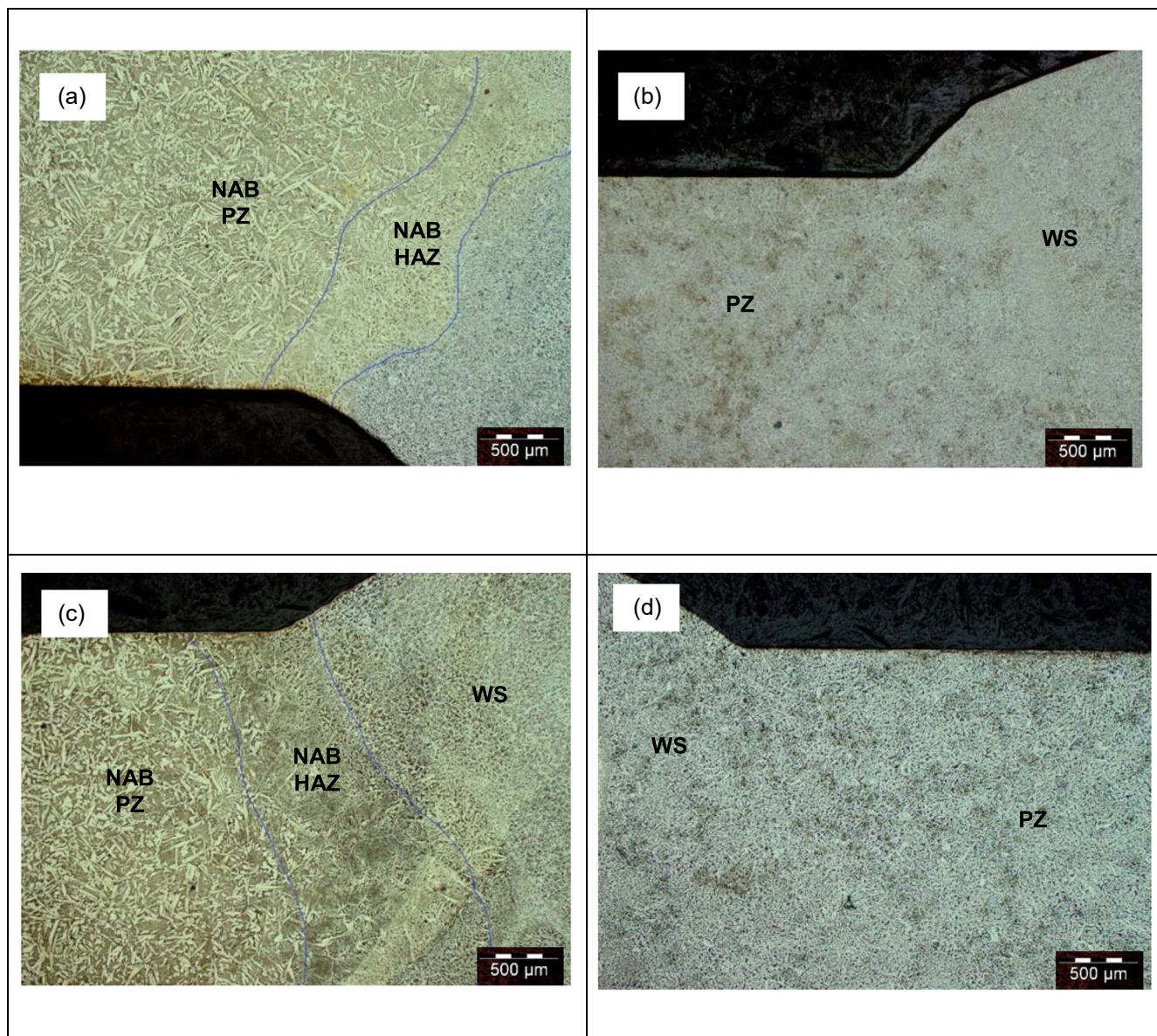


**FIGURE 4** LOM images after applying etchant 1 showing a general view of the microstructure of the NAB-MAB weld joint with ERCuMnNiAl filler: NAB area (a); MAB area (b); and with ERCuNiAl filler: NAB area (c); MAB area (d). LOM, light optical microscope; MAB, manganese aluminum bronze; NAB, nickel aluminum bronze. [Color figure can be viewed at [wileyonlinelibrary.com](https://onlinelibrary.wiley.com/doi/10.1002/maco.202213328)]

In comparison, the MAB-MAB weld joint does not exhibit a potential range with passivity, the current densities increase with increasing potential to high levels. (Figure 5b). At  $-100\text{ mV}_{\text{SCE}}$ , a current level at the upper limit of the instrument was reached and consequently, the series of test potentials was adjusted by 50 mV more negative for the hybrid weld joints.

Hybrid weld joints, NAB-MAB, show similar corrosion behavior with both filler metals (Figure 6a,b): cathodic state prevails at  $-300\text{ mV}_{\text{SCE}}$  and active corrosion at  $-150\text{ mV}_{\text{SCE}}$ , while at  $-250\text{ mV}_{\text{SCE}}$  rather low, steady corrosion current is established. At  $-200\text{ mV}_{\text{SCE}}$ , the currents tend to increase steadily with time, which is in general an indication of localized corrosion processes.

To further compare the corrosion behavior of NAB and MAB weld joints, the current densities after reaching the steady state may be considered, which not only reflect the tendency of the metal to dissolve but also include the ability of the material to develop protective layers of corrosion products. In view of the slow kinetics of copper alloys in reaching such a steady state, Table 2 compiles the final current densities after the full potentiostatic corrosion test duration of 72 h for all the weld joints in SSW. It can be highlighted that the results of NAB-NAB and MAB-MAB weld joints generally exhibit similar trends as were observed previously with unwelded, thermally treated NAB and MAB tested at the same potentials.<sup>[46]</sup>

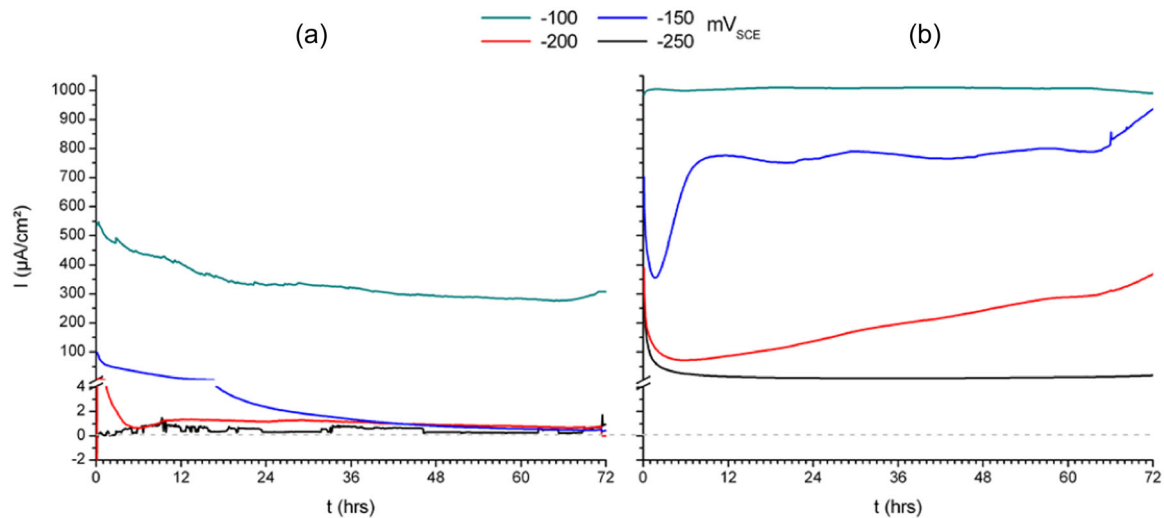


**FIGURE 5** Trends of current densities during potentiostatic corrosion testing of weld joints NAB-NAB (a) and MAB-MAB (b) in SSW. MAB, manganese aluminum bronze; NAB, nickel aluminum bronze; SSW, synthetic sea water. [Color figure can be viewed at [wileyonlinelibrary.com](https://onlinelibrary.wiley.com/doi/10.1002/maco.202213338)]

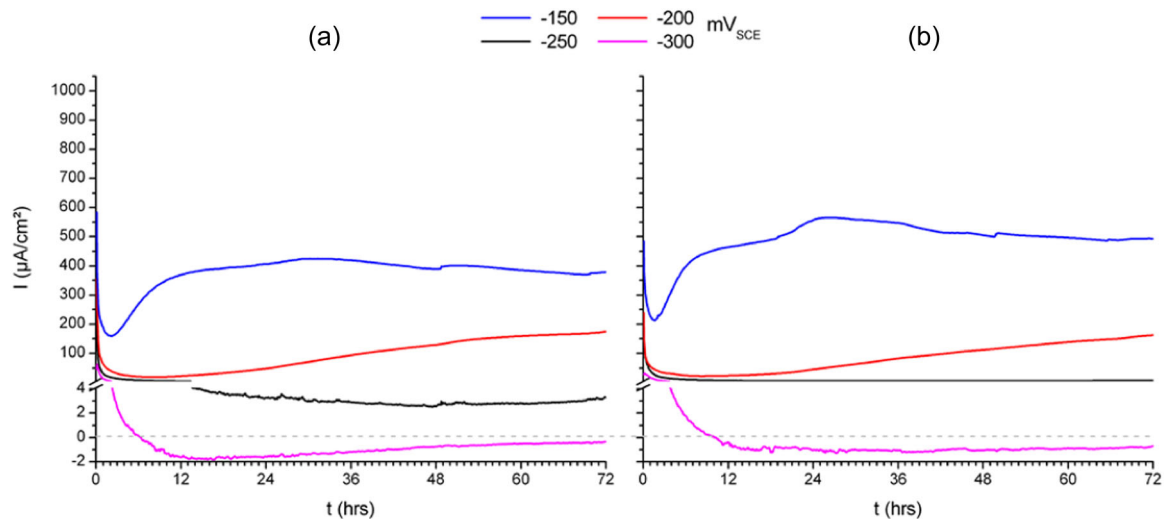


**FIGURE 6** Trends of current densities during on potentiostatic corrosion testing of NAB-MAB hybrid weld joints in SSW, ERcCuNiAl filler (a); ERcCuMnNiAl filler (b). MAB, manganese aluminum bronze; NAB, nickel aluminum bronze; SSW, synthetic sea water. [Color figure can be viewed at [wileyonlinelibrary.com](https://onlinelibrary.wiley.com/doi/10.1002/maco.202213338)]

**TABLE 2** Current density values ( $\mu\text{A}/\text{cm}^2$ ) for NAB and MAB welded coupons and exposed to SSW at various potentials, after 72-h of corrosion testing.

Joint	Filler metal	Test potential ( $\text{mV}_{\text{SCE}}$ )				
		-300	-250	-200	-150	-100
NAB-NAB	ERcCuNiAl	-	0.9	0.0	0.4	300
MAB-MAB	ERcCuMnNiAl	-	20	360	790	>1000
NAB-MAB	ERcCuNiAl	-0.3	3.3	174	380	-
	ERcCuMnNiAl	-0.7	7.0	162	492	-

Abbreviations: MAB, manganese aluminum bronze; NAB, nickel aluminum bronze.

With the NAB-NAB weld joint and by the end of the test (Table 2), low anodic current densities, that is, passive or cathodic behavior, were established at the lower test potentials, while the most positive potential resulted in two orders of magnitude higher anodic current reaching  $300 \mu\text{A}/\text{cm}^2$ . These data indicate a sharp transition from passive to active behavior in the potential interval of  $-150$  to  $-100 \text{ mV}_{\text{SCE}}$ . The MAB-MAB weld joint established a low yet significant current of  $20 \mu\text{A}/\text{cm}^2$  at  $-250 \text{ mV}_{\text{SCE}}$ , indicating corrosion involving a surface layer with some degree of protection. At more positive potentials, the final

current densities are much higher. Test results of hybrid NAB-MAB weld joints generally exhibit similar data as were observed with unwelded MAB samples<sup>[46]</sup> and with the MAB-MAB weld joint. Considering the MAB surface ratio in the hybrid joint is ca. 50% compared to the MAB-MAB joint, and by comparing the current densities in Table 2, we may conclude that the corrosion activity of the hybrid joints is dominated by the MAB side of the tested specimens. Moreover, there appears indication of an effect of the chemical composition of the filler metals in the hybrid joints at the test potential of  $-150 \text{ mV}_{\text{SCE}}$ : the joint with the

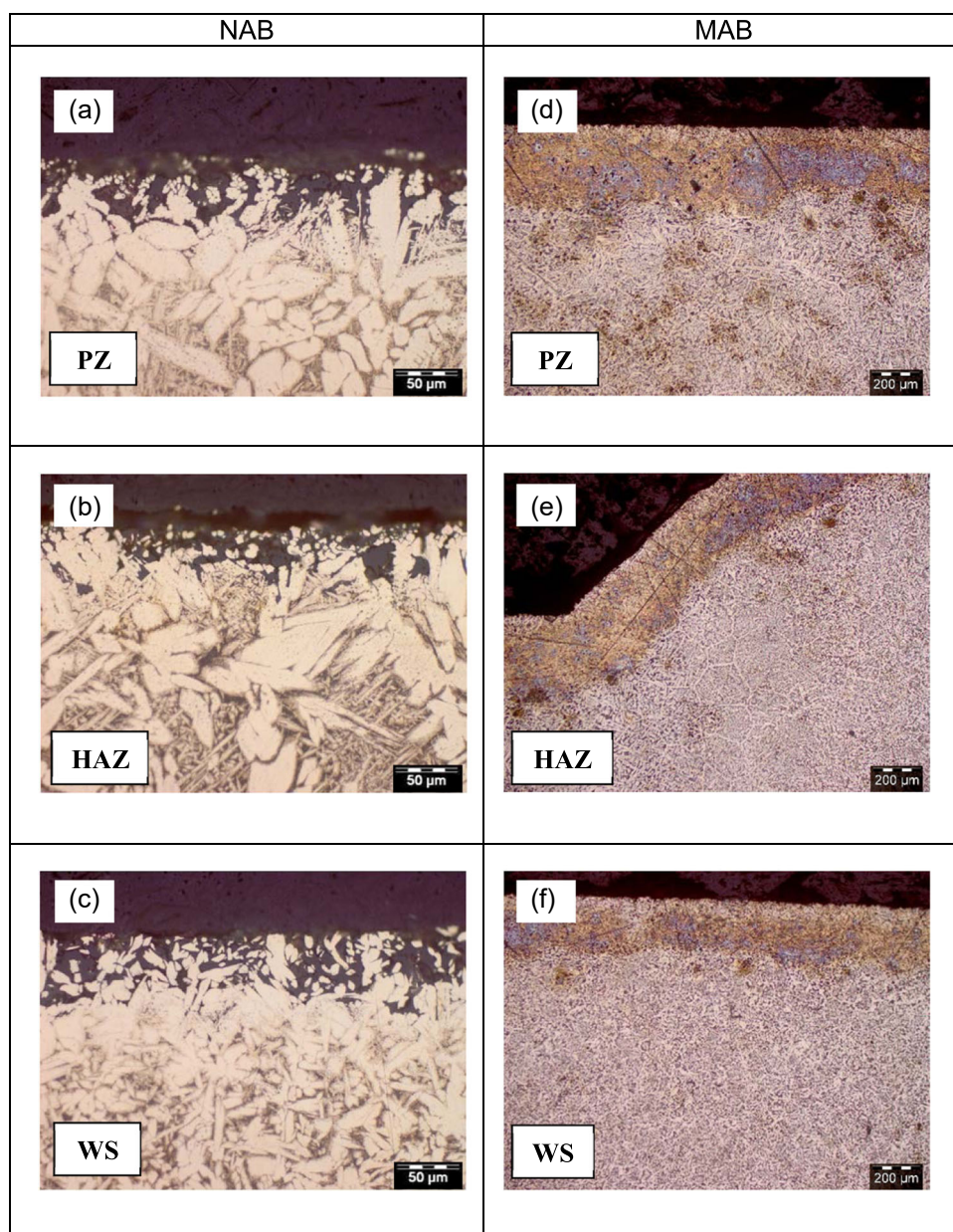


**FIGURE 7** LOM images of PZ, HAZ, and WS regions after potentiostatic corrosion testing in SSW for 72 h at  $-100 \text{ mV}_{\text{SCE}}$  for NAB and  $-150 \text{ mV}_{\text{SCE}}$  for MAB. Mind the different scales for NAB and MAB owing to the different depth of attack. HAZ, heat-affected zone; LOM, light optical microscope; MAB, manganese aluminum bronze; NAB, nickel aluminum bronze; PZ, parent zone; SEM, scanning electron microscope; WS, weld seam. [Color figure can be viewed at [wileyonlinelibrary.com](https://onlinelibrary.wiley.com/doi/10.1002/maco.202213328)]

ERCuNiAl filler established a lower current density ( $380 \mu\text{A}/\text{cm}^2$ ) compared to that with the ERCuMnNiAl filler ( $492 \mu\text{A}/\text{cm}^2$ ). This observation may be related again to the surface ratios of NAB, MAB, and filler. In the ERCuMnNiAl welded hybrid joint, MAB and the filler material have similar corrosion activity and thus their currents add up with a significant contribution of the filler. By contrast, with the ERCuNiAl welded hybrid joint, NAB and filler material remain rather passive and the observed current refers predominantly to the MAB surface only. The observed relationships between corrosion behavior and microstructure will be discussed in the following section.

### 3.3 | Characterization of the corroded surfaces

After the corrosion test, the cross sections of the samples were examined by LOM and SEM. Figure 7 presents the microstructures of PZ, HAZ, and WS regions after potentiostatic corrosion testing in SSW at  $-100 \text{ mV}_{\text{SCE}}$  for NAB and  $-150 \text{ mV}_{\text{SCE}}$  for MAB.

For NAB, selective corrosion of  $\beta$ -phase is clearly seen with a uniform depth of  $50 \mu\text{m}$  (Figure 7a–c). This coincides with partial dissolution of the large  $\alpha$ -phase dendrites while the  $\alpha$  Widmanstätten phase has disappeared. This partial attack on the  $\alpha$ -phase may be related to the relatively high test potential of  $-100 \text{ mV}_{\text{SCE}}$  in the transpassive range, at which all phases are attacked to some degree. The  $\beta$ -phase dissolves most quickly due to its chemical composition, and the  $\alpha$  Widmanstätten-phase disappears completely due to its fine needle structure. At the MAB specimen, a corroded brown layer with an average uniform thickness of about  $200 \mu\text{m}$  is observed in all the three identified zones with the typical appearance of dealloying (Figure 7d–f).

Figure 8 shows a SEM-BSE image of the attack on the HAZ of the NAB-NAB sample polarized at  $-100 \text{ mV}_{\text{SCE}}$ ,

and Table 3 presents the corresponding chemical composition from SEM/EDS analysis.

From Figure 8 and Table 3, it can be seen how spot 1, corresponding within the precision of this method to the  $\alpha$ -phase, shows a configuration of dendrites in the form of small needles with an interdendritic distance of approximately  $1\text{--}2 \mu\text{m}$ , indicating the partial dissolution of this phase. The corrosion products indicated in the picture are considered artifacts from preparing the cross-section. Liquid from the preparation has emerged from the crevices between the  $\alpha$  grains and caused the observed deposits. This phenomenon confirms the depth of the selective dissolution of the  $\beta$ -phase. At spot 2, where the previously  $\beta$ -phase was, the corrosion products are rich in Cu and with only a little amount of Al compared to the original alloy composition of this phase, which may be related to dealloying being involved in the corrosion attack. The  $\kappa$ -phase is located mostly inside the  $\alpha$ -phase and therefore shielded from corrosion. In cases of  $\kappa$ -phase got exposed to corrosion, this SEM/EDS analysis did not allow for assessing its possible reaction.

Figure 9 shows the HAZ SEM-BSE image, of the MAB-MAB sample polarized at  $-150 \text{ mV}_{\text{SCE}}$  and covers

TABLE 3 Chemical composition of the phases from EDS analysis (wt%) of NAB HAZ.

Area	Phase	Cu	Ni	Al	Fe	Mn
Noncorroded area	$\alpha$	84.35	2.94	7.37	3.29	1.19
	$\beta$	75.67	5.73	11.83	-	1.37
	$\kappa$	63.20	3.95	6.50	23.55	1.60
Corroded area	Spot 1	80.30	3.80	8.10	4.30	1.02
	Spot 2	81.90	2.15	0.90	-	-

Abbreviations: EDS, energy dispersive spectroscopy; HAZ, heat-affected zone; NAB, nickel aluminum bronze.

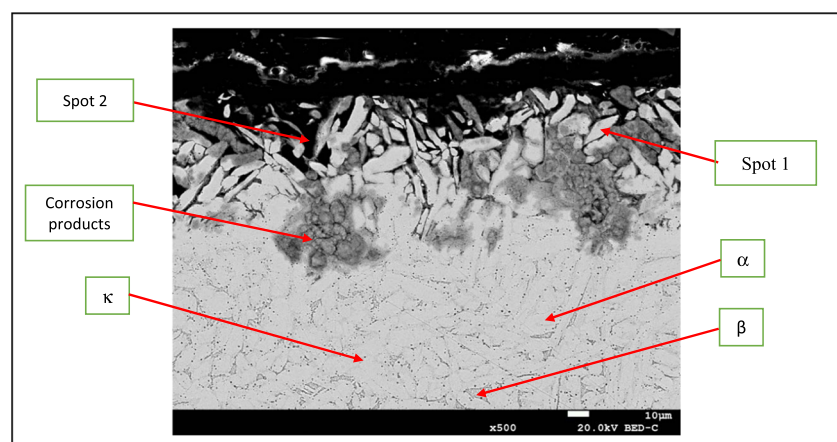
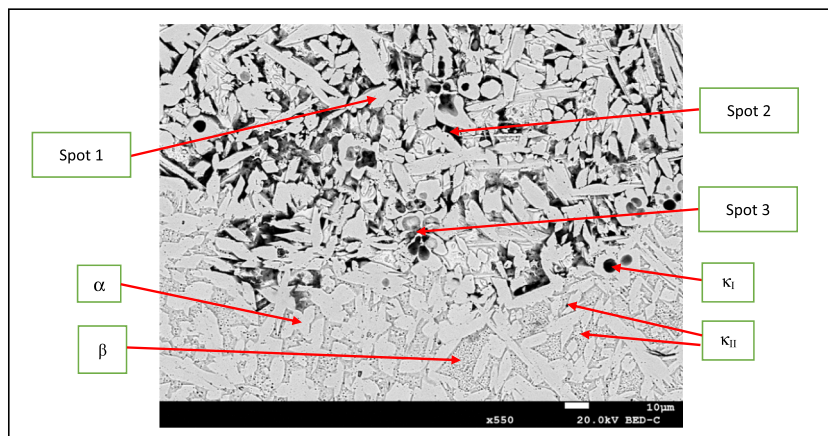


FIGURE 8 SEM image of NAB HAZ after potentiostatic corrosion testing in SSW for 72 h at  $-100 \text{ mV}_{\text{SCE}}$ . HAZ, heat-affected zone; NAB, nickel aluminum bronze; SEM, scanning electron microscope; SSW, synthetic sea water. [Color figure can be viewed at [wileyonlinelibrary.com](http://wileyonlinelibrary.com)]

**FIGURE 9** SEM image of MAB HAZ after potentiostatic corrosion testing in SSW for 72 h at  $-150\text{ mV}_{\text{SCE}}$ . HAZ, heat-affected zone; MAB, manganese aluminum bronze; SEM, scanning electron microscope; SSW, synthetic sea water. [Color figure can be viewed at [wileyonlinelibrary.com](http://wileyonlinelibrary.com)]



**TABLE 4** Chemical composition of the phases from EDS analysis (wt%) of MAB HAZ.

Area	Phase	Cu	Ni	Al	Fe	Mn	Zn
Noncorroded area	$\alpha$	73.00	1.80	5.90	3.50	11.90	2.30
	$\beta$	69.80	3.40	8.70	3.00	13.10	2.00
	$\kappa_I$	16.50	2.10	6.10	58.20	17.10	-
	$\kappa_{II}$	20.35	1.60	6.05	52.30	19.70	-
Corroded area	Spot 1	74.40	1.70	5.60	2.60	11.50	-
	Spot 2	83.60	0.85	1.00	0.60	2.50	-
	Spot 3	74.40	2.40	4.40	2.20	7.50	-

Abbreviations: EDS, energy dispersive spectroscopy; HAZ, heat-affected zone; MAB, manganese aluminum bronze.

the lower ca.  $150\ \mu\text{m}$  of the attacked surface layer is seen in Figure 7e. Table 4 presents the chemical composition from SEM/EDS analysis.

From Figure 9 and Table 4, selective corrosion of  $\beta$ -phase is observed. The analysis at spot 1, corresponding to the position where the  $\alpha$ -phase is, confirms that this phase remained intact. Spot 2, corresponding in this case to the location where the  $\beta$ -phase had dissolved, the corrosion products are dominated by Cu while the other elements are present at a much lower relative amount compared to the composition of the  $\beta$ -phase. These observations could be an indication of dealloying being part of the corrosion process. At spot 3, where the  $\kappa_I$ -phase got in contact with the electrolyte, Fe and Mn were removed and mainly Cu remained, indicating the dissolution of the  $\kappa_I$ -phase, possibly also via dealloying. In cases of  $\kappa_{II}$ -phase got exposed to corrosion, this SEM/EDS analysis did not allow for assessing its possible reaction.

## 4 | CONCLUSIONS

The main conclusions based on the experimental results and their analysis may be summarized as follows:

1. The investigated welded joints made of NAB and MAB are microscopically inhomogeneous due to the different structures and compositions of the PZ, HAZ, and WS. No significant influence of the filler metal was observed, the ERCuNiAl behaves similar to the NAB and ERCuMnNiAl similar to the MAB.
2. The  $\beta$ -phase is most sensitive against corrosion and undergoes selective corrosion, which was observed in both alloys. This is particularly critical when the amount of  $\beta$ -phase is increased by the welding process, as was observed for HAZ in NAB. In general,  $\alpha$ -phase does not corrode in NAB with the exception of high test potential in the transpassive range, at which  $\alpha$ -phase dendrites partially dissolve and the fine needles of  $\alpha$  Widmanstätten disappear. In MAB, however, dissolution of the  $\kappa_I$ -phase was observed in the WS.
3. Potentiostatic corrosion tests of NAB-MAB hybrid weld joint in SSW indicated that the corrosion processes are dominated by the MAB, being the critical material in such an assembly under enhanced corrosion conditions. Consequently, in the particular case of repair welding of NAB components, the match of the filler metal and the base material is important.

4. Possible postwelding heat treatments should have the goal of minimizing the amount of  $\beta$ -phase, enlarging the  $\alpha$ -phase grains, and avoiding wide zones of  $\alpha$  Widmanstätten structure.

## ACKNOWLEDGMENTS

The authors would like to acknowledge the company Wärtsila Ibérica, S.A. located in Maliaño, Cantabria, Spain, for providing materials and continuous support during all the analysis. This study was supported by Programa de Doctorados Industriales of Universidad de Cantabria, Spain (Grant No. 03.DI07.649). CRUE/G-9 hybrid - Universidad de Cantabria.

## CONFLICT OF INTEREST

The authors declare no conflict of interest.

## DATA AVAILABILITY STATEMENT

Research data are not shared.

## ORCID

Ignacio Cobo  <http://orcid.org/0000-0002-6684-3671>

Maria V. Biezma-Moraleda  <https://orcid.org/0000-0002-0709-7656>

Paul Linhardt  <http://orcid.org/0000-0002-4523-2185>

## REFERENCES

- [1] J. Birn, I. Skalski, presented at EUROCORR **2004**, Nice, France, 12–16 September 2004.
- [2] A. Schüssler, H. E. Exner, *Corr. Sc.* **1993**, *34*, 1793.
- [3] P. J. Macken, A. A. Smith, *The Aluminum Bronzes: Properties and Production Processes*, Copper Development Association, London, UK **1966**.
- [4] J. C. Park, M. S. Han, S. J. Kim, *Surf. Interface Anal* **2012**, *44*, 11.
- [5] D. Harsha Varhan, A. Ramesh, B. Chandra Mohan Reddy, *Mater Today: Proc.* **2019**, *18*, 4482.
- [6] A., Couture, *ASF Int. Cast. Met. J.* **1981**, *6*, 33.
- [7] C. H. Tang, F. T. Cheng, *Surf. Coat. Technol.* **2006**, *200(8)*, 2602.
- [8] J. M. Hobbs, ASTM STP 408. Erosion by Cavitation or Impingement. American Society for Testing and Materials: West Conshohocken, PA, USA, **1967**, p. 220. <https://www.scribd.com/document/477276297/ASTM-STP-408-Erosion-by-Cavitation-or-Impingement> [accessed March 2022].
- [9] R. Thomson, J. O. Edwards, *AFS Transact.* **1978**, *86*, 395.
- [10] G. W. Lorimer, F. Hasan, J. Iqbal, N. Ridley, *Br. Corros. J.* **1986**, *21*, 244.
- [11] F. Hasan, A. Jahanafrooz, G. W. Lorimer, N. Ridley, *Metall. Trans. A* **1982**, *13A*, 1337.
- [12] J. A. Wharton, K. R. Stokes, *Electrochim. Acta* **2008**, *53*, 2463.
- [13] J. A. Wharton, R. C. Barik, G. Kear, R. J. K. Wood, K. R. Stokes, F. C. Walsh, *Corros. Sci.* **2005**, *47*, 3336.
- [14] A. Al-Hashem, W. Riad, *Mater. Character.* **2002**, *48*, 37.
- [15] P. J. Macken, A. A. Smith, *The Aluminum Bronzes: Properties and Production Processes*, Copper Development Association, London, UK **1966**.
- [16] B. Sabbaghzadeh, R. Parvizi, A. Davoodi, M. H. Moayed, *Mater. Des.* **2014**, *58*, 346.
- [17] H. Li, D. Grudgings, N. Larkin, J. Norrish, M. Callagan, L. Kuzmikova, *Mater. Sci. Forum* **2012**, *706*, 2980.
- [18] X. Y. Li, Y. G. Yan, L. Ma, Z. M. Xu, J. G. Li, *Mater. Sci. Eng. A* **2004**, *382*, 82.
- [19] P. Punburi, N. Tareelap, N. Srisukhumbowornchai, V. Yordsri, *Mater. Chem. Phys.* **2018**, *212*, 471.
- [20] C. H. Tang, F. T. Cheng, H. C. Man, *Mat. Sci. Eng. A-Struct.* **2004**, *373*, 195.
- [21] H. Meigh, *Cast and Wrought Aluminium Bronzes Properties, Processes and Structure*, IOM Communications Ltd., London, UK **2000**.
- [22] J. Iqbal, F. Hasany, F. J., *Mater. Sci. Technol.* **2006**, *22*, 779.
- [23] N. Tareelap, K. Sriraksasin, C. Nitipanyawong, P. Termsuksawad, *KKU Eng.* **2013**, *40*, 561.
- [24] Z. Han, Y. F. He, H. C. Lin, H. Zhao, *J. Mater. Sci. Lett.* **2000**, *19*, 393.
- [25] W. Liu, S. Zhang, N. Li, J. Zheng, S. An, Y. Xing, *Int. J. Electrochem. Soc.* **2012**, *7*, 2240.
- [26] P. Punburi, N. Tareelap, N. Srisukhumbowornchai, C. Euaruksakul, V. Yordsri, *Appl. Surf. Sci.* **2018**, *439*, 1040.
- [27] N. M. Mota, S. S. M. Tavares, A. M. Do Nascimento, G. Zeeman, M. V. Biezma-Moraleda, *Eng. Fail. Anal.* **2021**, *129*, 105732.
- [28] Z. Han, H. Zhao, *Mater. Sci. Eng. A* **2003**, *345*, 8.
- [29] X. Y. Li, Y. G. Yan, L. Ma, Z. M. Xu, J. G. Li, *Mater. Sci. Eng. A* **2004**, *382*, 82.
- [30] Q. N. Son, Y. G. Zheng, D. R. Ni, Z. Y. Ma, *Corros. Sci.* **2015**, *92*, 95.
- [31] J. Frei, B. T. Alexandrov, M. Rethmeier, *Weld. World* **2016**, *60*, 459.
- [32] S. Chen, D. K. L. Tsang, L. Jiang, K. Yu, C. Li, Z. Li, Z. Li, X. Zhou, J. Yang, *Mat. Sci. Eng A-Struct.* **2017**, *699*, 48.
- [33] H. S. Khatak, B. Raj, *Corrosion of Austenitic Stainless Steels: Mechanism, Mitigation and Monitoring*, Narosa Publishing House, India **2002**.
- [34] Y. Ma, X. Zhou, Y. Liao, Y. Yi, H. Wu, Z. Wang, W. Huang, *Corros. Sci.* **2016**, *107*, 41.
- [35] R. Dong, J. Li, T. Zhang, R. Hu, K. Kou, *Mater. Character.* **2016**, *122*, 189.
- [36] Y. Ma, X. Zhou, W. Huang, Y. Liao, X. Chen, X. Zhang, G. E. Thompson, *Corros. Eng. Sci. Techn.* **2015**, *50*, 420.
- [37] A. Suzuki, Y. Mishin, *Interface Sci* **2003**, *11*, 131.
- [38] M. G. McPhie, S. Berbenni, M. Cherkaoui, *Comput. Mater. Sci.* **2012**, *62*, 169.
- [39] Q. Luo, Z. Wu, Z. Qin, L. Liu, W. Hu, *Surf. Coat. Technol.* **2017**, *309*, 106.
- [40] C. Herzig, S. V. Divinski, *Mater. Trans.* **2003**, *44*, 14.
- [41] G. F. Vander Voort, *Metallography: Principles and Practice*, 3rd ed., ASM International, Materials Park, OH, USA **2004**.
- [42] J. R. Davis, *Copper and Copper Alloys*, ASM International, Materials Park, OH, USA **2001**.
- [43] P. Linhardt, S. Kühner, G. Ball, M. V. Biezma, *Mater. Corros.* **2017**, *69*, 358.

- [44] X. Y. Li, Y. G. Yan, L. Ma, Z. M. Xu, J. G. Li, *Mater. Sci. Eng. A* **2004**, 382, 82.
- [45] M. R. Mirzadeh Rahni, B. Beidokhti, M. Haddad-Sabzevar, *Trans. Nonferrous Met. Soc. China* **2017**, 27, 507.
- [46] P. Linhardt, S. Strobl, J. Böhm, R. Haubner, M. V. Biezma, *Pract. Metallogr.* **2021**, 58, 72.

**How to cite this article:** I. Cobo, M. V. Biezma-Moraleda, P. Linhardt, *Mater. Corros.* **2022**;73:1788–1799.  
<https://doi.org/10.1002/maco.202213328>